Dual-Energy Cone-Beam CT with Three-Material Decomposition for Bone Marrow Edema Imaging

Stephen Z. Liu,[a] Magdalena Herbst,[b] Thomas Weber,[b] Sebastian Vogt,[b] Ludwig Ritschl,[b]
Steffen Kappler,[b] Jeffrey H. Siewerdsen,[a] and Wojciech Zbijewski[a,*]

[a]Department of Biomedical Engineering, Johns Hopkins University, Baltimore, MD 21205
[b]Siemens Healthineers, Forchhelm 91301, Germany

ABSTRACT

We investigate the feasibility of bone marrow edema (BME) detection using a kV-switching Dual-Energy (DE) Cone-Beam CT (CBCT) protocol. This task is challenging due to unmatched x-ray paths in the low-energy (LE) and high-energy (HE) spectral channels, CBCT non-idealities such as x-ray scatter, and narrow spectral separation between fat (bone marrow) and water (BME). We propose a comprehensive DE decomposition framework consisting of projection interpolation onto matching LE and HE view angles, fast Monte Carlo scatter correction with low number of tracked photons and Gaussian denoising, and two-stage three-material decompositions involving two-material (fat-Aluminium) Projection-Domain Decomposition (PDD) followed by image-domain three-material (fat-water-bone) base-change. Performance in BME detection was evaluated in simulations and experiments emulating a kV-switching CBCT wrist imaging protocol on a robotic x-ray system with 60 kV LE beam, 120 kV HE beam, and 0.5° angular shift between the LE and HE views. Cubic B-spline interpolation was found to be adequate to resample HE and LE projections of a wrist onto common view angles required by PDD. The DE decomposition maintained acceptable BME detection specificity (<0.2 mL erroneously detected BME volume compared to 0.85 mL true BME volume) over +/-10% range of scatter magnitude errors, as long as the scatter shape was estimated without major distortions. Physical test bench experiments demonstrated successful discrimination of ~20% change in fat concentrations in trabecular bone-mimicking solutions of varying water and fat content.

Keywords: dual-energy CT, cone-beam CT, multi-material decomposition, quantitative imaging, bone marrow edema.

***Wojciech Zbijewski, E-mail: wzbijewski@jhu.edu**

1. INTRODUCTION

Bone trauma is often accompanied by bone marrow edema (BME), which presents as elevated fluid content within the fatty yellow marrow. BME detection is conventionally performed using MRI. However, there has been an increasing interest in BME detection using x-ray CT because of its ubiquity in the emergency department, where the presence of BME might aid the diagnosis of occult fractures[1,2]. Since the x-ray attenuation alone is insufficient to distinguish relative contributions of fat, water and bone to trabecular bone voxels, dual-energy (DE) imaging with three-material decomposition have been proposed for BME identifications, e.g., using a dual-source CT[3]. Here, we investigate the feasibility of DE BME imaging on Flat-Panel Detector (FPD) Cone-Beam CT (CBCT) with the kV-switching protocol.

The primary challenge in DE detection of BME is the narrow energy separation between fat and water-like soft-tissues. Thus, any imaging system biases need to be carefully controlled. This is particularly challenging in CBCT due to its sensitivity to x-ray scatter and detector non-idealities (e.g., glare). We propose a BME imaging framework based on a DE CBCT protocol where the kV changes every 0.5° gantry angle (corresponding to a ~50 ms switching interval). The projections are processed with fast Monte Carlo (MC)-based scatter corrections[4], resampled onto matching view angles, and input into the two-material (fat-Aluminum) Projection-Domain Decomposition (PDD) followed by the three-material (fat-water-cortical bone) image-domain base-change[5,6]. We used both simulations and CBCT benchtop experiments to evaluate impact of scatter estimation errors and other CBCT system non-idealities on the performance of the proposed DE BME imaging framework.

7th International Conference on Image Formation in X-Ray Computed Tomography,
edited by Joseph Webster Stayman, Proc. of SPIE Vol. 12304, 123040Z

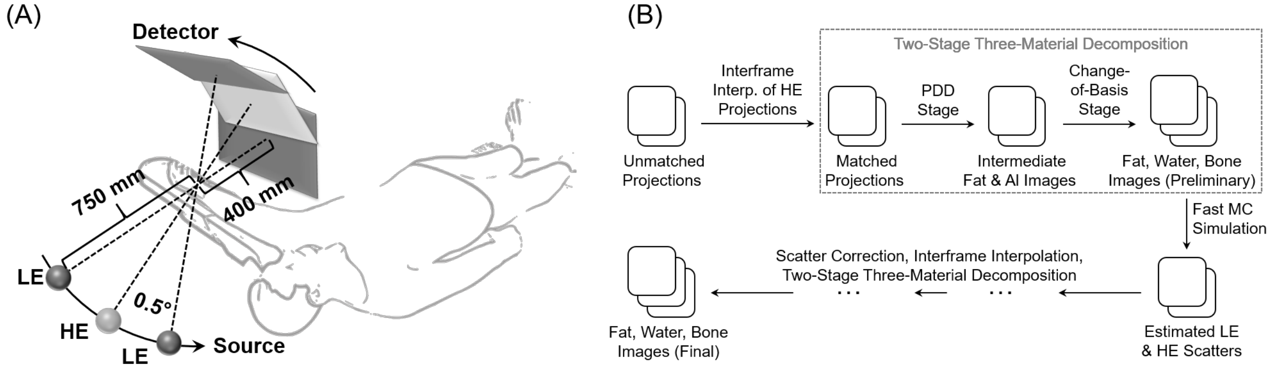

Figure 1. (A) The wrist CBCT scan geometry and the kV-switching protocol. (B) Thee-material (water-fat-bone) DE decomposition framework for the kV-switching CBCT.

2. METHOD

2.1 kV-Switching DE CBCT of the Wrist

Simulations and benchtop experiments emulated the Siemens Healthineers Multitom Rax twin robotic x-ray system in the wrist CBCT configuration shown in Fig. 1A. The source-axis distance was 750 mm, and the source-detector was 1150 mm. We investigated a realistic kV-switching DE protocol where the x-ray source alternated between the low-energy (LE) beam of 60 kV (+2 mm Al, +0.25 mm Cu) and the high-energy (HE) beam of 120 kV (+2 mm Al, +0.25 mm Cu) every 0.5° views, yielding a total 200 LE and 200 HE frames over 200° rotation.

2.2 Three-Material DE Decomposition

We applied a two-stage three-material DE decomposition method in Yu et al[5] (Fig. 1B). First, PDD was performed by interpolating the precomputed 2D lookup tables to convert DE projections into line integrals of two intermediate bases – fat and Al. This step minimized the effects of beam hardening. Reconstructions of fat and Al line integrals were then obtained and processed with base-change to produce the final fat, water and cortical bone volume fraction maps.

Throughout all studies, fat and Al reconstructions involved the FDK algorithm with 0.5 x 0.5 x 0.5 mm^3 voxels, Parker weighting, and 2D ramp kernel (0.5x Nyquist frequency cutoff and Hann apodization). The base-change was formulated as the least-square minimization problem constrained by the volume conservation principle[7,8], and optimized using the active-set algorithm. 10 iterations of 3D total-variation denoising with 0.8 penalty strength were applied to the resulting material images.

The kV switching protocol did not provide coinciding LE and HE ray paths required by PDD, due to 0.5° angular separation between successive LE and HE projection views. Therefore, HE projections at the gantry angles matching the LE projections were synthesized using the sinogram interframe interpolation; various interpolation approaches were compared (see Sec. 3).

Scatter correction was achieved by a previously developed fast MC-based approach[4]. A rapid, but relatively noisy MC simulation with a low number of tracked photons was first performed; the scatter estimate was then denoised using a 2D Gaussian kernel and subtracted from the projections. The object model for the MC simulation was given by the material maps obtained from a preliminary three-material decomposition of the uncorrected data. A second, final pass of the decomposition was then applied to the corrected projections (see Fig. 1B).

2.3 Simulation Studies

The sensitivity of proposed framework in Fig. 1B to scatter estimation errors was investigated using a previously reported realistic x-ray system model[9]. We assumed a 400 x 400 mm2 FPD with 0.3 x 0.3 mm^2 pixel size and a 0.6 mm thick CsI scintillator. The x-ray source was operated at 4 mAs/frame for the 60 kV beam, and 1 mAs/frame for the 120 kV beam. X-ray spectra and linear attenuation coefficients of all materials were obtained from Spektr3.0[10]; quantum and detector electronic noise with correlations were included in the model. Source axial collimation was set to 150 mm (on the

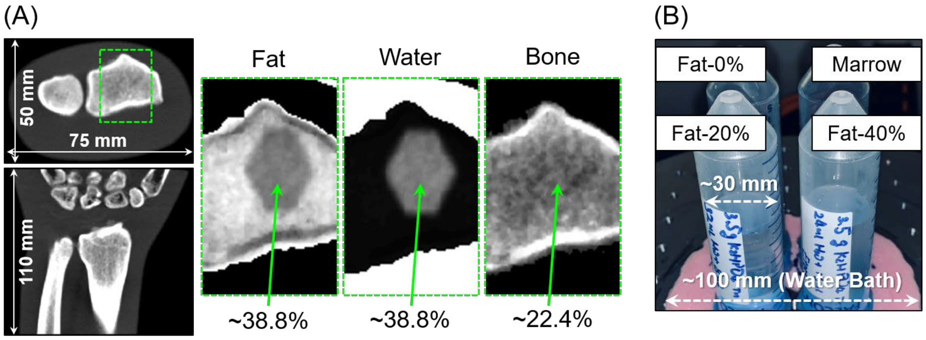

Marrow	40 mL **EtOH**
Fat-40%	3.5 g **K_2HPO_4** in 24 mL **H_2O** + 16 mL **EtOH**
Fat-20%	3.5 g **K_2HPO_4** in 32 mL **H_2O** + 8 mL **EtOH**
Fat-0%	3.5 g **K_2HPO_4** in 40 mL **H_2O**

Figure 2. (A) FDK reconstruction of digital normal wrist phantom. Material fraction maps in the BME region (green box) are shown on the right. Volume fractions are provided for each material. (B) Physical phantom consisting of a water cylinder (not shown) with four vials containing the H_2O-EtOH-K_2HPO_4 mixtures specified in the table.

detector). No anti-scatter grid was installed. Ground truth scatter was simulated using the MC algorithm with a relatively large number of photon tracks (10^7) and minimal smoothing (kernel FWHM = 4 mm).

We used two digital anthropomorphic phantoms: a normal wrist of ~50 x 75 mm^2 cross section shown in Fig. 2A, and a large wrist obtained by dilating the soft tissues of the normal wrist to ~80 x 105 mm^2 cross section. The wrists consisted of an outer fat layer (skin), an inner water region (soft tissues), and bones made of a mixture of cortical bone and fat (yellow marrow). A ~0.85 mL BME stimulus containing cortical bone and equal fractions of fat and water was placed in the radius (Fig. 2A). All mixtures fulfilled the volume conservations.

2.4 Sensitivity to Scatter Correction Errors

Simulated kV-switching data were processed following the pipeline in Fig. 1B. Fast MC scatter estimation was performed using 106 photons (Fig. 3) – an order of magnitude less than the ground truth in data generation (107). We studied the sensitivity of decomposition to inaccuracies in i) shape and ii) magnitude of the estimated scatter. The shape error was introduced by adjusting FWHM of the Gaussian smoothing kernel (ranging 10 - 290 mm), which introduced an increasing distortion of the scatter as illustrated in Fig. 3. The magnitude error was generated by scaling the denoised scatter distribution (ranging 80% - 120%). A total of 9x9 combinations of errors were tested.

The performance of decompositions under scatter inaccuracy was evaluated in terms of the specificity of BME detection. We measured whether any connected water voxel clusters >1.5 mm diameter were present in the bones where there should be no fluid – i.e., outside of the true BME stimulus. To this end, the non-zero water voxels within bone boundaries were segmented; the segmentation was then processed with erosion followed by dilation using a 1.5 mm diameter sphere to remove any clusters <1.5 mm diameter. Detection specificity was computed as: $V_{detected} - V_{detected \cap true}$, where $V_{detected}$ is the total volume of water detected (segmented) within bones, and $V_{detected \cap true}$ is the volume of water detected within the true BME region.

2.5 Physical CBCT Test Bench Study

CBCT test bench equipped with a 300 x 300 mm^2 FPD with 0.388 x 0.388 mm^2 pixels was configured to emulate Multitom Rax wrist scan geometry as in the simulations, with 60 mm axial collimation on the detector. The same DE acquisition protocol as in the simulations was implemented.

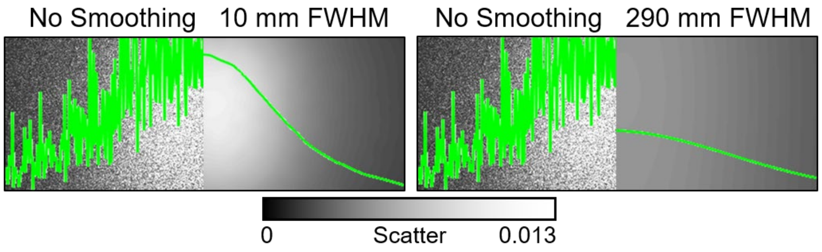

Figure 3. MC-estimated LE scatter profiles using 10^6 photon tracks without smoothing, and with 10 mm and 290 mm FWHM Gaussian kernels. Green curves show the scatter profile along the central detector row.

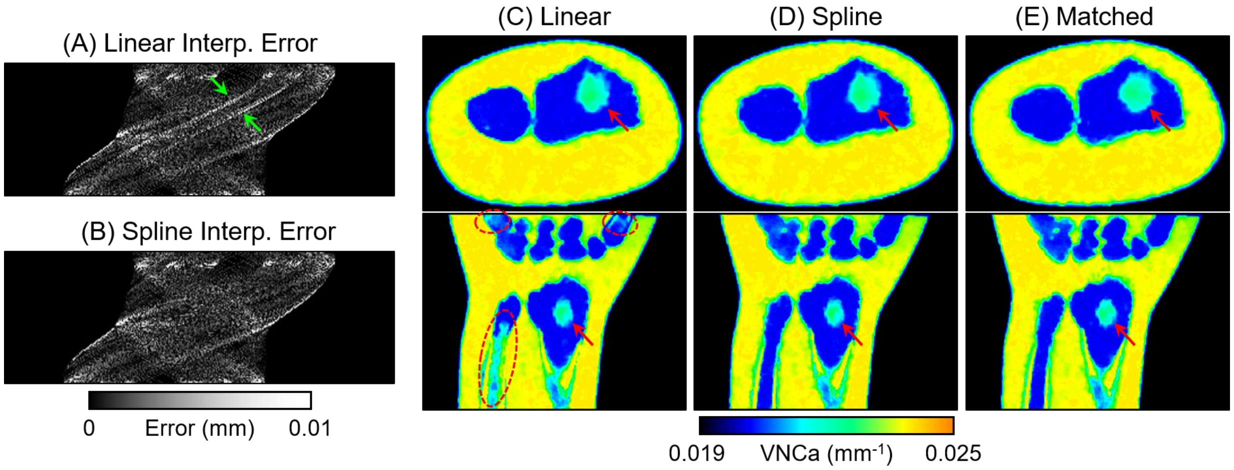

Figure 4. Absolute sinogram errors for linear (A) and spline (B) interframe interpolations of HE data. The errors are plotted for the detector row approx. 200 slices inferior from the central slice. Green arrows indicate the error on the ulna. Decompositions (VNCa images) for DE acquisitions of unmatched LE/HE projections with linear (C) and spline (D) interframe interpolations, and of matched LE/HE projections (idealized reference) (E). Red arrows indicate the true BME region; red dashed circles mark the false BME enhancement.

A three-material physical phantom was developed to validate BME detection, as shown in Fig. 2B. Ethyl alcohol (EtOH) was used to represent yellow marrow, H_2O for soft-tissue and BME, and K_2HPO_4 for cortical bone. The phantom consisted of a ~100 mm diameter water bath with 4 Falcon® tubes of ~30 mm diameter. The composition in each tube is listed in Fig. 2B.

Detector glare deconvolution[4] was performed on the DE projections prior to applying the two-stage DE decomposition framework of Sec. 2.2. Fast MC scatter estimation used 106 photons and a 10 mm FWHM smoothing kernel. The PDD stage used polyethylene (PE) and Al as bases; in the base-change stage, they were converted to EtOH, H_2O and K_2HPO_4 bases. Spectra for PDD lookup tables were calibrated from attenuation measurements of Al filters of varying thickness. In the base-change stage, the span of PE-Al that formed each of the final material was obtained from the PDD of a calibration phantom different from the phantom used in the study.

3. RESULTS

Fig. 4 provides a comparison of two different interframe interpolation kernels for synthesizing HE projections at view angles matching the LE data: 2D linear and cubic B-spline. (Note that in this test, the projection data was scatter-free.) The interpolations were applied onto the sinogram of each detector row separately. The differences from a reference HE sinogram simulated directly at the view angles of the LE scan are shown in Fig. 4A for the linear interpolation, and in Fig. 4B for the B- spline interpolation. The decompositions for the two synthesis techniques are displayed as the Virtual Non-Calcium images (VNCa – the attenuation-weighted sum of decomposed fat and water images[11,12]) as in Fig. 4C and 4D. Linear interpolation introduced false BME signals in the ulna and metatarsals, likely due to the sharp transitions in the sinogram of these regions. B-spline interpolation, on the other hand, was free of such errors, indicating that it is an adequate choice for angular resampling of the sinogram. A reference reconstruction of the simulation with matched LE and HE frames is provided in Fig. 4E. Spline projection view synthesis was applied in the subsequent studies.

Fig. 5A shows the VNCa images of the normal wrist for selected combinations of scatter magnitude and shape errors. BME (water) >1.5 mm that were detected in the bones (i.e., true and false positives) are marked. Fig. 5B and C present the BME detection specificity across investigated scatter estimation error settings for the normal and large wrist. Clear visualizations of BME and high detection specificity (<0.2 mL false detection volume compared to 0.85 mL true BME volume) was achieved for both normal and large wrists when the magnitude error was within +/-10% range. This, however, required that the scatter shape was estimated without any major distortions (smoothing FWHM <80 mm). The large wrist was more sensitive to scatter correction inaccuracies, consistent with its elevated scatter-to-primary ratio (SPRs for the normal wrist at the detector center were 6.5% and 4.6% for LE and HE frames, respectively, compared to 14.4% and 10.1% for the large wrist). Fig. 6 shows the axial and coronal VNCa images for the large wrist using scatter simulation with 10 mm FWHM smoothing and 0% introduced magnitude error. There are almost no false BME clusters outside of the true stimulus, illustrating the feasibility of DE CBCT of BME providing adequate scatter correction.

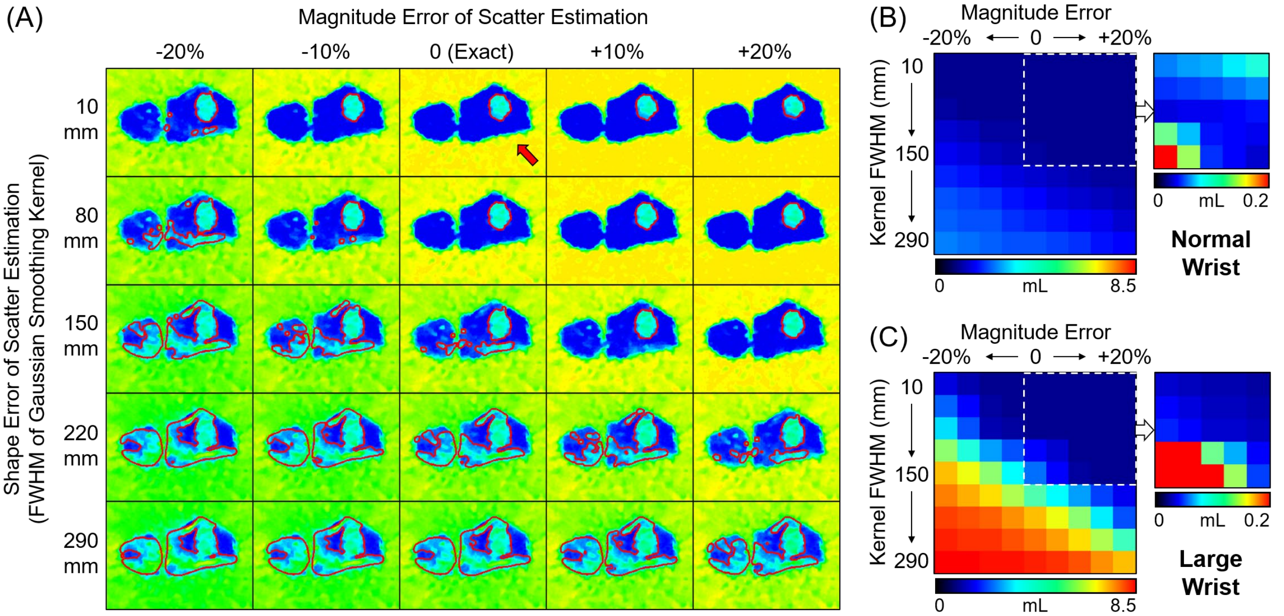

Figure 5. (A) Axial VNCa images (cropped around the bone region) for the scatter error study of the large wrist. Red contours mark the detected BME regions (both true and false positives). (B) BME detection specificity across all scatter error cases for the normal wrist. The region in the dashed box is also shown using a narrower error range. (C) Same as (B) for the large wrist.

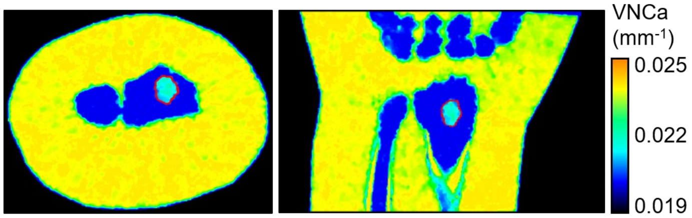

Figure 6. Decomposition of the large wrist scan for MC scatter correction with 0% magnitude error and the 10 mm FWHM Gaussian smoothing kernel. Red contours mark the detected BME areas.

Fig. 7A shows the FDK reconstruction of test-bench LE acquisitions of the physical phantom. The variation in fat (i.e., EtOH) fractions among inserts (less fat – more BME) cannot be appreciated on the attenuation image, but is readily apparent in the DE decompositions with proper artifact corrections. The DE decomposition without glare or scatter correction (Fig. 7B) presents erroneous fat content in the fat-free insert (Fat-0%) and underestimated water concentrations in the water bath. These errors are largely removed with scatter correction (Fig. 7C). Fig. 7D underscores the need for the correction of FPD non-idealities – the VNCa image with glare and scatter correction achieves improved uniformity in the water bath than the image without glare correction.

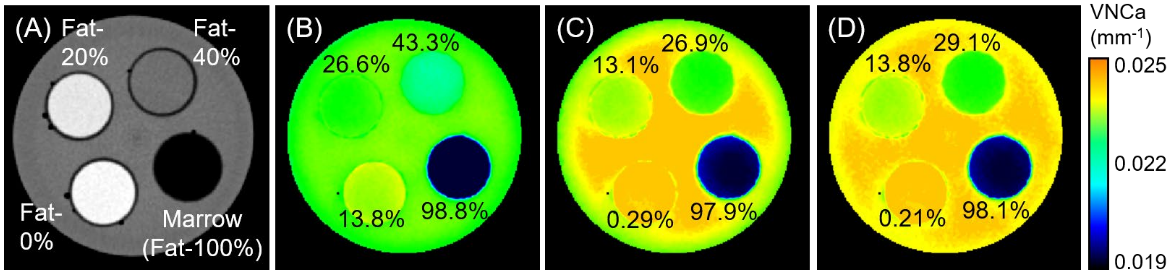

Figure 7. (A) FDK reconstruction of the test-bench LE projections of the physical BME phantom. The ground truth fat (EtOH) fraction in each insert is marked. VNCa images of decomposition with no corrections (B), without glare correction but with scatter correction (C), and with both glare and scatter corrections (D). Estimated fat fractions for each case are indicated.

4. DISCUSSION & CONCLUSION

We investigated the feasibility of BME detection using the kV-switching DE CBCT protocol paired with an analytical two-stage three-material decomposition pipeline. The problem is inherently challenging due to unmatched x-ray paths of the LE and HE channels and similar attenuation properties of fat-like yellow marrow and water-like BME.

Using high-fidelity simulations, we found that the B-spline interpolation is sufficient to resample HE and LE frames onto common view angles required by PDD from an acquisition with a 0.5º shift between the two spectral channels. This result was achieved for the fairly complex anatomy of the wrist, indicating that spline projection synthesis might be useful in a broad range of kV-switching CBCT applications. Considering inaccuracies of scatter estimation, the decomposition maintains acceptable BME detection specificities over +/-10% magnitude errors as long as scatter shape is reasonably accurate. This finding suggests that MC or deep learning-based scatter corrections are likely adequate for BME detection using DE CBCT.

The feasibility of BME detections using proposed DE CBCT framework was validated in physical test bench experiments, demonstrating successful estimation of the difference in fluid and fat content of trabecular bone-mimicking solutions.

Ongoing works include experimental reproducibility study in complex objects under variable imaging conditions[13], and the application of a recently reported model-based one-step DE three-material decomposition algorithm (CMBMD)[8] to BME quantification to avoid interframe interpolations.

5. ACKNOWLEDGEMENT

This work was supported by academic-industrial collaboration with Siemens Healthineers, XP Division, and by NIH R01 EB025470. The presented method in not commercially available. Due to regulatory reasons, Siemens Healthineers Multitom Rax in not available in all countries, and its future availability cannot be guaranteed.

REFERENCE

[1] Ali, I. T., Wong, W. D., Liang, T., Khosa, F., Mian, M., Jalal, S., and Nicolaou, S., “Clinical utility of dual-energy CT analysis of bone marrow edema in acute wrist fractures,” American Journal of Roentgenology, 210(4), 842-847 (2018).

[2] Gosangi, B., Mandell, J. C., Weaver, M. J., Uyeda, J. W., Smith, S. E., Sodickson, A. D., and Khurana, B., “Bone marrow edema at dual-energy CT: a game changer in the emergency department,” Radiographics, 40(3), 859-874 (2020).

[3] Petritsch, B., Kosmala, A., Weng, A. M., Krauss, B., Heidemeier, A., Wagner, R., Heintel, T. M., Gassenmaier, T., and Bley, T. A., “Vertebral compression fractures: third-generation dual-energy CT for detection of bone marrow edema at visual and quantitative analyses,” Radiology, 284(1), 161-168 (2017).

[4] Sisniega, A., Zbijewski, W., Xu, J., Dang, H., Stayman, J. W., Yorkston, J., Aygun, N., Koliatsos, V., and Siewerdsen, J. H., “High-fidelity artifact correction for cone-beam CT imaging of the brain,” Physics in Medicine & Biology, 60(4), 1415 (2015).

[5] Yu, L., Liu, X., and McCollough, C. H, “Pre-reconstruction three-material decomposition in dual-energy CT,” In Medical Imaging 2009: Physics of Medical Imaging, Vol. 7258, pp. 1218-1225 (2009).

[6] Liu, S. Z., Zhao, C., Herbst, M., Weber, T., Vogt, S., Ritschl, L., Kappler, S., Siewerdsen, J. H., and Zbijewski, W., “Feasibility of dual-energy cone-beam CT of bone marrow edema using dual-layer flat panel detectors,” In Medical Imaging 2022: Physics of Medical Imaging, Vol. 12031, p. 120311J (2022).

[7] Barber, R. F., Sidky, E. Y., Schmidt, T. G., and Pan, X., “An algorithm for constrained one-step inversion of spectral CT data,” Physics in Medicine & Biology, 61(10), 3784 (2016).

[8] Liu, S. Z., Siewerdsen, J. H., Stayman, J. W., and Zbijewski, W., “Quantitative dual-energy imaging in the presence of metal implants using locally constrained model-based decomposition,” In Medical Imaging 2021: Physics of Medical Imaging, Vol. 11595, p. 115951C (2021).

[9] Zhao, C., Liu, S. Z., Wang, W., Herbst, M., Weber, T., Vogt, S., Ritschl L., Kappler, S., Stayman J. W., Siewerdsen, J. H., and Zbijewski, W., “Effects of x-ray scatter in quantitative dual-energy imaging using dual-layer flat panel detectors,” In Medical Imaging 2021: Physics of Medical Imaging, Vol. 11595, p. 115952A (2021).

[10] Punnoose, J., Xu, J., Sisniega, A., Zbijewski, W., and Siewerdsen, J. H., "spektr 3.0—A computational tool for x-ray spectrum modeling and analysis," Medical physics, 43(8Part1), 4711-4717 (2016).

[11] Kellock, T. T., Nicolaou, S., Kim, S. S., Al-Busaidi, S., Louis, L. J., O'Connell, T. W., Ouellette, H. A., and McLaughlin, P. D., "Detection of bone marrow edema in nondisplaced hip fractures: utility of a virtual noncalcium dual-energy CT application," Radiology, 284(3), 798-805 (2017).

[12] Müller, F. C., Gosvig, K. K., Børgesen, H., Gade, J. S., Brejnebøl, M., Rodell, A., Nemery, M., and Boesen, M., "Dual-energy CT for suspected radiographically negative wrist fractures: a prospective diagnostic test accuracy study," Radiology, 296(3), 596-602 (2020).

[13] Liu, S. Z., Cao, Q., Osgood, G. M., Siewerdsen, J. H., Stayman, J. W., and Zbijewski, W., "Quantitative assessment of weight-bearing fracture biomechanics using extremity cone-beam CT," In Medical Imaging 2020: Biomedical Applications in Molecular, Structural, and Functional Imaging, Vol. 11317, p. 113170I (2020).